



**HAL**  
open science

## On the role of the mesoscale circulation on an idealized coastal upwelling ecosystem

Cyril Lathuilière, Vincent Echevin, Marina Lévy, Gurvan Madec

### ► To cite this version:

Cyril Lathuilière, Vincent Echevin, Marina Lévy, Gurvan Madec. On the role of the mesoscale circulation on an idealized coastal upwelling ecosystem. *Journal of Geophysical Research*, 2010, 115, pp.09018. 10.1029/2009JC005827 . hal-00758856

**HAL Id: hal-00758856**

**<https://hal.science/hal-00758856>**

Submitted on 3 Nov 2021

**HAL** is a multi-disciplinary open access archive for the deposit and dissemination of scientific research documents, whether they are published or not. The documents may come from teaching and research institutions in France or abroad, or from public or private research centers.

L'archive ouverte pluridisciplinaire **HAL**, est destinée au dépôt et à la diffusion de documents scientifiques de niveau recherche, publiés ou non, émanant des établissements d'enseignement et de recherche français ou étrangers, des laboratoires publics ou privés.

Copyright

## On the role of the mesoscale circulation on an idealized coastal upwelling ecosystem

C. Lathuilière,<sup>1,2</sup> V. Echevin,<sup>1</sup> M. Lévy,<sup>1</sup> and G. Madec<sup>1</sup>

Received 22 September 2009; revised 12 April 2010; accepted 3 May 2010; published 18 September 2010.

[1] An idealized circulation model of coastal upwelling coupled to an ecosystem model has been built to address the impact of features such as eddies and filaments emerging from mesoscale dynamics on a marine ecosystem. The model mimics coastal upwelling along an infinite straight coast with north–south cyclic boundary conditions. Thanks to the parametrization of the geostrophic onshore flow in the thermocline, the circulation captures the typical characteristics of a coastal upwelling region: an equatorward coastal jet, a poleward undercurrent along the continental slope and mesoscale eddies and filaments. This eddying three-dimensional simulation is compared to a two-dimensional simulation using the averaged velocity field of the first simulation as velocity field. This approach allows us to compare simulations having similar upwelling and nutrient input but differing in the nature of the flow. An offshore spreading of the phytoplankton bloom is found in the eddying simulation. The width of the productive coastal band is increased from 80 km to 200 km by the mesoscale activity. A biogeochemical budget carried out in a 300 km-wide coastal band provides evidence that mesoscale activity decreases the total phytoplankton content mainly by exporting a significant part of the surface phytoplankton below the euphotic layer. In presence of mesoscale activity, the downward and offshore export of phytoplankton, zooplankton and detritus significantly contributes to total export of organic matter out of the surface coastal ocean, whereas their contribution to export is weak in the two-dimensional case.

**Citation:** Lathuilière, C., V. Echevin, M. Lévy, and G. Madec (2010), On the role of the mesoscale circulation on an idealized coastal upwelling ecosystem, *J. Geophys. Res.*, 115, C09018, doi:10.1029/2009JC005827.

### 1. Introduction

[2] Ecosystems in eastern boundary upwelling system are well known for their high productivity [Carr and Kearns, 2003]. In those regions, alongshore winds drive coastal upwelling. The associated vertical flux of nutrient enhances primary production near the shore. A sharp contrast is therefore observed between the cold chlorophyll-rich coastal area and the warmer more oligotrophic chlorophyll-poor open ocean.

[3] Eastern boundary upwelling systems (EBUSs) are also characterized by the presence of an unstable coastal jet [McCreary et al., 1991; Barth, 1994; Durski and Allen, 2005]. Meanders of the jets and eddies emerge from the baroclinic instability of the jet and contribute to the strong mesoscale activity observed in EBUSs. An intense surface eddy kinetic energy has indeed been estimated both from satellite-derived geostrophic velocity and from model studies in most of the EBUSs [Marchesiello et al., 2003;

Penven et al., 2005; Lathuilière et al., 2008]. Other processes contribute to this high mesoscale activity, such as for instance the radiation of the coastal jet into Rossby waves and the propagation of coastal trapped waves [Philander and Yoon, 1982].

[4] This mesoscale activity has a strong impact on biological activity as shown by ocean color images. At large scales (O(100–1000 km)), ocean color images show that the coastal regions are chlorophyll-rich [Carr and Kearns, 2003; Lathuilière et al., 2008]. At mesoscale scale (O(10–100 km)), patchy chlorophyll distributions are collocated with dynamical structures. The most noticeable feature is the high chlorophyll concentration in upwelling filaments [Chavez et al., 1991; Bricaud et al., 1987; Van Camp et al., 1991]. An anti-correlation is observed between horizontal mixing and surface chlorophyll [Rossi et al., 2008].

[5] Nevertheless, the main parameters affecting the structure and the richness of ecosystems in EBUSs are clearly the parameters controlling the Ekman transport and the nutrient input. In particular, the properties of the upwelled waters such as the initial nitrate concentration strongly impact the nutrient input. The upwelling mass flux is also a key parameter. The Ekman transport drives an offshore drift of surface waters and thus plays a major role in the offshore extension of coastal nitrogen-rich waters. Primary

<sup>1</sup>LOCEAN, Institut Pierre-Simon Laplace, Université Pierre et Marie Curie, CNRS, IRD, MNHN, Paris, France.

<sup>2</sup>REC, HOM, SHOM, Brest, France.

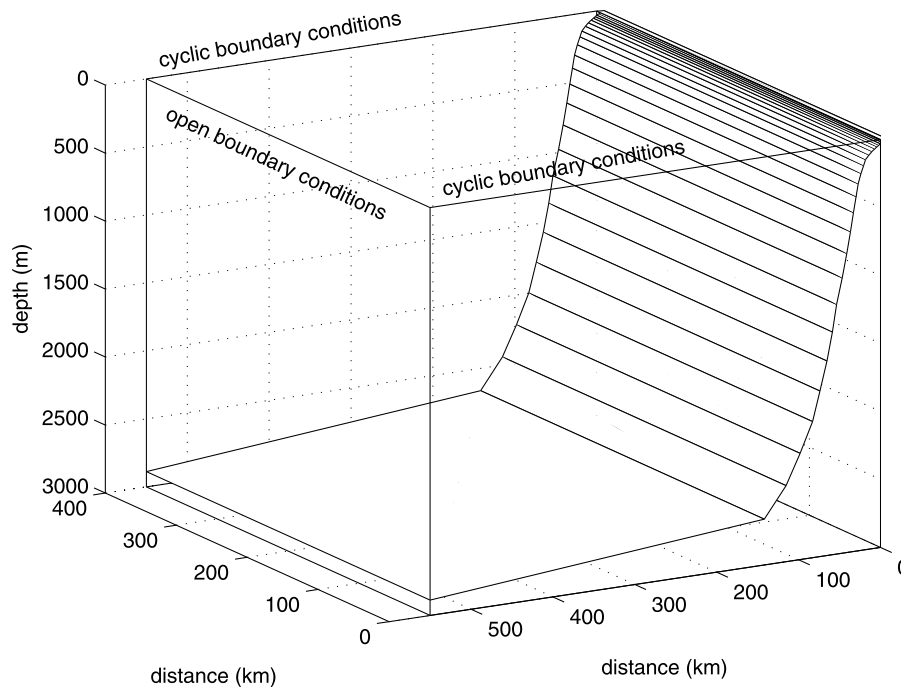


**Figure 1.** Bathymetry as a function of the distance from the coast. The vertical levels are projected on the bottom topography.

production is also modulated by the mixed layer depth. Those parameters define key environmental conditions for EBUSs ecosystems. However, is the knowledge of those parameters sufficient to determine the main characteristics of ecosystem? How sensitive is the ecosystem to the exchanges emerging from the mesoscale dynamics?

[6] To answer these questions, the approach we use in this study is to compare simulations having very similar environmental conditions but differing by the presence or the absence of mesoscale activity. By similar environmental conditions, we mean that either simulation has similar mixed layer depth, intensity of Ekman transport, upwelling mass flux, depth of the onshore current in subsurface and nutrient richness in upwelled waters. Those forcings are expected to be the main factors controlling the primary production in EBUSs. The simulation including mesoscale circulation is a three-dimensional eddying simulation. The simulation excluding mesoscale circulation is a two-dimensional simulation obtained by using the Eulerian mean flow of the first simulation to advect the biogeochemical tracers in the ecosystem model. Hence, the properties of the upwelled waters, the upwelling mass fluxes and the nutrient input are very similar in the two simulations. On the contrary, they mainly differ by the complex two-way and intermittent vertical and horizontal fluxes generated by the mesoscale circulation.

[7] An idealized model has been used to reduce the complexity of the analysis. Indeed, the comparison between realistic three-dimensional models [Spitz *et al.*, 2005; Gruber *et al.*, 2006] and two-dimensional models [Edwards *et al.*, 2000; Spitz *et al.*, 2003] is complex, since they differ not only by the presence of surface two-way offshore-onshore exchanges but also by the alongshore variation of mean properties as for instance the alongshore currents and by the propagation of remote forcing by coastal trapped waves.

[8] This paper is organized as follows. In section 2, the model and diagnostics used for the analysis are presented. In section 3, we first give an overview of the mean circulation and of the dynamic structures. Then we compare the two simulations. A biogeochemical budget is carried out to measure the differences of averaged properties within the 300 km wide coastal region. Finally, section 4 emphasizes the role and the nature of the eddy fluxes and conclusions are presented in section 5.

## 2. Methods and Model Setting

### 2.1. Physical Model

[9] The ocean circulation model we use is NEMO v2 (Nucleus for European Modelling of the Ocean, second version) [Madec *et al.*, 1998; Madec, 2008]. This primitive-equation ocean model is formulated in z-coordinates with partial steps at the bottom [Pacanowski and Gnanadesikan, 1998]. Tracer and momentum are advected using the TVD advection scheme, which ensures positivity for the tracer concentrations [Zalesak, 1979; Lévy *et al.*, 2001a]. Horizontal diffusion for momentum and tracers uses a bi-harmonic operator, with diffusivity and viscosity coefficients set to  $-5.10^9 \text{ m}^2/\text{s}$ . The vertical mixing scheme is a TKE parameterization [Blanke and Delecluse, 1993]. The horizontal grid is regular and the grid spacing is  $1/12^\circ$ , which is sufficient to resolve the mesoscale dynamics. The domain zonal width is 500 km and its meridional extension is 400 km. The thickness of the 30 vertical levels varies from 225 m at the bottom to 4 m at the surface. The bottom topography is uniform alongshore. It includes a shelf, a continental slope and further offshore a flat bottom at 3000 m representing an alongshore average topographic profile for the Northwest African coast (Figure 1).

[10] The idealized configuration mimics the ocean circulation along a straight meridionally-oriented coast, and uses North–South cyclic boundary conditions. This type of boundary conditions preclude large scale alongshore gradients. In particular, the Coriolis factor is necessarily constant. Its value corresponds to a latitude of approximately 20°N and to an inertial period of 36 hours. Moreover, the large scale alongshore pressure gradient associated with the density field is necessarily nil, preventing any onshore-offshore mean geostrophic velocity. Under such conditions, the mean onshore-offshore velocities are therefore ageostrophic and mainly occur in the Ekman surface layer, in the bottom frictional layer and in the interior of the ocean through nonlinear momentum flux [Lentz and Chapman, 2004]. Thus, the offshore horizontal water flux in the surface Ekman layer is balanced by a onshore transport in the bottom frictional layer [Allen *et al.*, 1995; Spitz *et al.*, 2003]. However, observations of temperature and salinity of upwelled waters indicate that they were initially at a depth of around 100–150 m [Carr and Kearns, 2003], suggesting that the onshore current is localized in the thermocline. An alongshore pressure gradient driving an onshore geostrophic current is thus necessary in theoretical coastal upwelling models [Hurlburt and Thompson, 1973]. The modeling experiments of the Californian EBUS confirm the geostrophic nature of the onshore flow [Capet *et al.*, 2008]. Thus, in order to faithfully mimic this subsurface circulation in the present model, an alongshore pressure-gradient is added to the pressure gradient derived from the density field. This prescribed alongshore pressure gradient is adjusted to drive a more realistic onshore transport, which compensates the Ekman transport. This transport is vertically distributed between 44m and 198m in the core of the thermocline below the maximum mixed layer depth.

[11] The surface heat and salt fluxes are determined by using the CLIO bulk formulae [Madedec, 2008]. All fields that enter the bulk formulae are set to annual mean spatially uniform values. In particular, they do not include a seasonal cycle. The air temperature, the 10-m wind speed, the specific humidity, the cloud cover and the precipitation are derived from the COADS climatology along the northwest African coast at 20°N. The wind stress is alongshore-oriented and set to 0.075 N/m<sup>2</sup>, the annual mean value of alongshore QuikSCAT wind stress in this region [Lathuilière *et al.*, 2008].

[12] Open boundary conditions (hereafter OBC) are imposed at the western boundary of the basin [Treguier *et al.*, 2001]. The OBC algorithm combines a radiation condition with a relaxation to a reference data set. The inflow or outflow condition is determined from  $c_n$ , an Orlandi-type phase velocity [Treguier *et al.*, 2001]. In case of inflow, the OBC is a relaxation to boundary data with a 40-day time scale. In case of outflow, an advection term is computed using  $c_n$  as the velocity across the boundary. This algorithm requires boundary data including temperature, salinity and normal velocity. In this study, the boundary temperature and salinity are those of the initial state and the normal velocity at the boundary is determined from the interior velocity by continuity, allowing the Ekman transport and the subsurface compensating flow across the open boundary. A sponge layer with an harmonic viscosity of 200 m<sup>2</sup>/s is applied within 80 km from the open boundary to damp the artificial

propagation of near-inertial waves from the open boundary into the model domain.

[13] An internal damping is applied on the temperature and salinity field to reach a steady state within a reasonable time. Let us consider a model variable  $\phi$ , which can be either temperature or salinity, its alongshore mean  $\bar{\phi}$  and the reference field  $\phi_r$ . The term used for the damping is the following:

$$\frac{\partial \phi}{\partial t} = -\frac{1}{\tau}(\bar{\phi} - \phi_r)$$

[14] This Newtonian damping calculated on the alongshore mean field has no impact on the alongshore anomalies. Note that traditional Newtonian damping is generally proportional to  $\phi - \phi_r$ , which damps the anomalies. The time scale  $\tau$  is 100 days below 150 m, increases above 150m and there is no damping above 55 m. The reference fields are the initial temperature and salinity fields.

## 2.2. Ecosystem Model

[15] The physical model is coupled with the 6-component nitrogen-based ecosystem model LOBSTER [Lévy *et al.*, 2005; Krémeur *et al.*, 2009]. It includes one phytoplankton and one zooplankton. It explicitly resolves the new primary production (NPP) and the regenerated primary production (RPP) defined as the nitrate and ammonium uptakes, respectively. The two other variables are the dissolved organic matter (DOM) and the detritus (DET). The ecosystem model uses the same diffusion and advection scheme as the physical model for salinity and temperature. A restoring term is imposed to the nitrate concentration below the euphotic depth, preventing any long time scale drift of nitrate concentration.

[16] The parameterizations used for the biogeochemical source and sink terms (SMS) are presented in Appendix A. Most of the biogeochemical parameters are identical to those of Krémeur *et al.* [2009]. They have been chosen to mimic the ecosystem dynamics in the north Atlantic ocean over a wide range of ecosystem behaviors. In the present study, the phytoplankton and zooplankton maximal growth rate have been chosen to fit with coastal upwelling ecosystem [Spitz *et al.*, 2003]. The half-saturation rate of ammonium ( $K_{NH_4}$ ) was set to 0.1 to be more consistent with modeling experiment in EBUS [Spitz *et al.*, 2005]. The nitrate field was initialized with climatological value from World Ocean Atlas (2001, [http://www.nodc.noaa.gov/OC5/WOA01/pr\\_woa01.html](http://www.nodc.noaa.gov/OC5/WOA01/pr_woa01.html)). The others components were initialized with a low and constant value of 0.1 mmolN/m<sup>3</sup>.

## 2.3. Methods

[17] Two simulations are analyzed and compared. The first one is the so-called 3-D simulation, performed on the previously described three-dimensional grid. It includes mesoscale circulation. An anomaly of 0.001°C has been added to the initial temperature field in one grid cell in order to trigger the development of the mesoscale instabilities. A spin-up of 4 years has been performed and the fifth year has been analyzed.

[18] In the second simulation called 2-D, the ecosystem model has been run off-line on a two-dimensional grid

(cross-shore vertical slice), forced by the Eulerian mean circulation of 3-D. For this purpose, the physical outputs of 3-D have been temporally and alongshore averaged. Note that the average have been carried out along geopotential contours. The average of the 3-D field along isopycnal coordinates has been examined, but it leads to an underestimation of the mixed layer depth. The initial state of the ecosystem model has been set to the alongshore-mean initial state of 3-D. A 2-year run has been performed. The first year is necessary to reach the equilibrium state, and the second year is analyzed in this paper. In this off-line simulation, the vertical mixing coefficient has been separately computed because of its highly non-linear behavior. A median operator in the alongshore dimension and then in time has been applied on the vertical mixing coefficient to provide a steady two-dimensional vertical mixing coefficient field. The use of a median operator provides a realistic nitracline in the off-line simulation, whereas an arithmetic mean leads to a too deep nitracline (not shown). Note that a similar approach has been used to determine the most representative mixed layer depth out of a set of vertical temperature and salinity profiles [de Boyer Montégut et al., 2004].

[19] The budget for the 6 biogeochemical components has been carried out in the surface coastal region. For this purpose, we define a coastal transition zone (CTZ) box as the 300 km wide coastal band in the depth range 0–55 m. This box is designed to encompass the vertical variations of the mixed layer and the horizontal extension of the upwelling filaments. Every contribution to the evolution of the biogeochemical tracers is quantified within the CTZ box. The most significant terms are analyzed in this study, including advection across the box boundaries, vertical diffusion and the sources minus sinks biogeochemical terms. The other terms including horizontal diffusion, dilution by rainfall, other minor numerical effects and the total trend associated with the variations of stocks have been added together and presented as the “other” term (Figure 6).

[20] The advective fluxes  $\overline{u_i \cdot c}$  are now decomposed into mean and eddy contributions:

$$\overline{u_i \cdot c} = \overline{u_i} \cdot \overline{c} + \overline{u_i' \cdot c'}$$

[21] In this definition,  $u_i$  is the velocity field in the direction  $i$  and  $c$  is the tracer field. A given field  $c$  is decomposed into a mean state  $\overline{c}$  and an anomaly  $c'$ . The mean state is defined as the annual and meridional mean over the fifth year of simulation, taken along constant depth surfaces. Practically, the Reynolds-averaged fluxes  $\overline{u_i' \cdot c'}$  have been diagnosed as  $\overline{u_i \cdot c} - \overline{u_i} \cdot \overline{c}$ .  $\overline{u_i \cdot c}$  has been saved online from the advection routine, while  $\overline{u_i} \cdot \overline{c}$  has been estimated off-line using the same advection scheme, since  $\overline{u_i}$  and  $\overline{c}$  are only known at the end of the simulation.

### 3. Results

#### 3.1. Flow Structure and Biogeochemical Response

[22] In this part, the results of the 3-D simulation are described. We investigate how the simulation reproduces the coastal upwelling circulation and the ecosystem. Finally snapshots of physical and biogeochemical fields are used to describe the mesoscale circulation.

#### 3.1.1. Mean Flow Structure

[23] In this section, we examine the vertical and cross-shore structure of the flow and temperature field. First, let us consider the onshore-offshore circulation and the vertical velocity. Because of the cyclic boundary conditions, the meridional mean flow is non-divergent, which allows to define a stream function on a cross-shore vertical slice. The obtained upwelling overturning cell is presented on Figure 2a. The circulation within the surface layer is driven by the Ekman flow and its associated transport is fairly constant from 30 km to 400 km of the coast. Vertical transport occurs within a nearshore 30 km wide coastal band corresponding to 3 grid points. Below 50m depth, we observe the onshore compensating flow, driven by the imposed alongshore pressure gradient [See section 2.1].

[24] The imposed alongshore pressure gradient and the corresponding geostrophic flow allow the upwelled waters to have realistic properties. The 18°C isotherm outcrops at the coast and is located at 100 m depth 400 km offshore from the coast (Figure 2b). The depth of the upwelling source water is thus 100 m which is consistent with what has been observed in various EBUSs [Carr and Kearns, 2003]. The difference between the SST 400 km offshore and the SST at the coast is approximately 4°C, in agreement with observations [Nykjaer and Van Camp, 1994]. A shoaling of the isotherms is observed in a 250 km wide coastal band. The isotherm slope is weak except within the 30 km wide coastal region, where coastal upwelling occurs and isotherms steepen.

[25] The alongshore velocity exhibits a typical structure for coastal upwelling. At the surface near the coast, a coastal equatorward jet balances the cross-shore pressure gradient due to the shoaling and outcropping of the isopycnals. The width and depth of the coastal jet is 30 km and 30–40 m respectively. The maximal equatorward velocity within the coastal jet is 20 to 30 cm/s. Below the coastal jet along the slope, a poleward undercurrent driven by the alongshore pressure gradient, is 30 km wide and located below 50m. The poleward velocity reaches 20 cm/s. This picture of a coastal jet and a poleward undercurrent fits well with the Canary EBUS observations [Barton, 1998]. Further offshore, the alongshore circulation is weak.

#### 3.1.2. Mean Biogeochemical Fields

[26] Figure 3 shows a time and meridional mean cross-shore section of the 6 biogeochemical fields within the upper 100 m in the 3-D simulation. Mean isopycnals have been superimposed on the biogeochemical fields to compare them with the physical structure. We also indicate the 0.005 mmolN/m<sup>3</sup>/d isoline of primary production as a proxy of the euphotic depth. In response to the nutrient input at the coast, a phytoplankton bloom occurs in the mixed layer. The phytoplankton concentration reaches 4 mmolN/m<sup>3</sup> within the upper 20m in a 100 km-wide coastal band. Below the euphotic depth, from 0 to 120 km offshore, the phytoplankton concentration exceeds 0.3 mmolN/m<sup>3</sup>, the phytoplankton concentration in the mixed layer 300 km offshore. It can already be hypothesized that the phytoplankton found below the euphotic depth was not produced locally but has been imported from the euphotic layer. We will come back to this point in section 4.

[27] As for phytoplankton, the highest zooplankton concentration is found within the mixed layer and above the

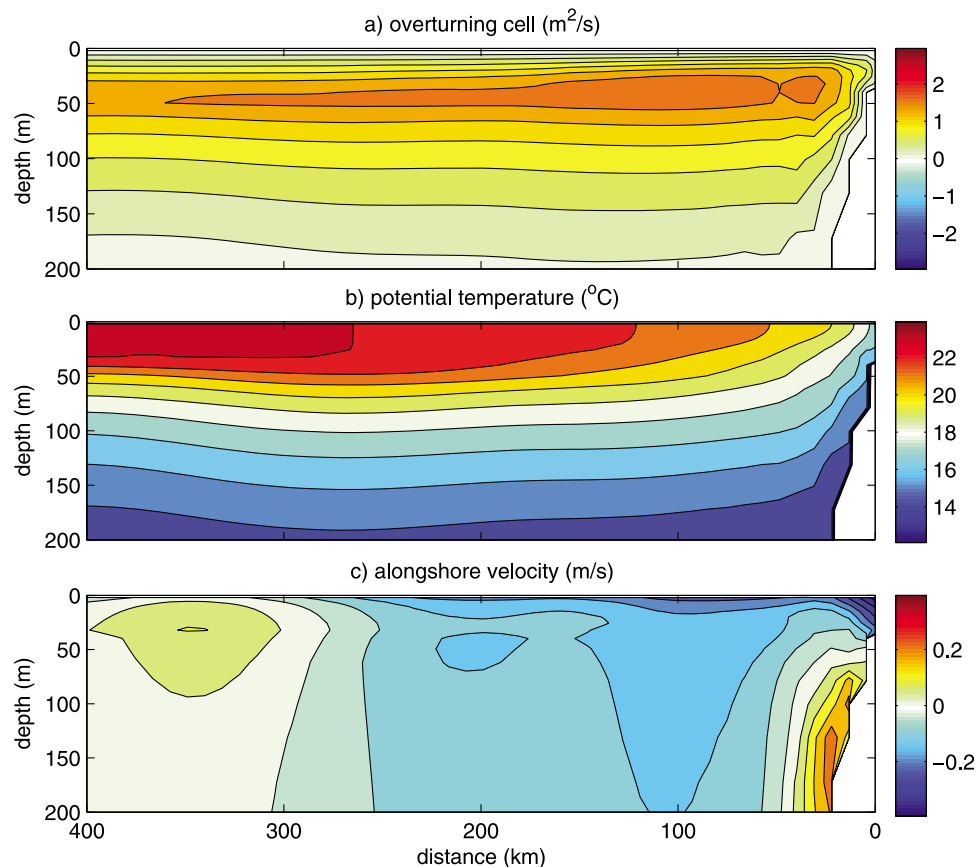


**Figure 2.** (a) Overturning cell computed from the alongshore-mean velocity field. (b) Alongshore-mean potential temperature field. (c) Alongshore-mean alongshore velocity (positive velocities are poleward). The data originate from the fifth year.

euphotic depth. It reaches  $0.9 \text{ mmolN/m}^3$  from 20 km to 100 km from the coast. It decreases further offshore to reach  $0.3 \text{ mmolN/m}^3$  400 km offshore. Conversely to phytoplankton, a significant part of the zooplankton stock is located below the euphotic depth. This is mainly due to the grazing of sinking detritus. At a depth of 80 m, zooplankton concentration remains relatively high ( $0.3 \text{ mmolN/m}^3$ ) compared to the surface value within 100 km from the coast.

[28] The nitrate concentration exhibits a sharp contrast between the low concentration at the surface (less than  $1 \text{ mmolN/m}^3$ ) and the rich subsurface (more than  $10 \text{ mmolN/m}^3$  below 50 m). The impact of coastal upwelling is clearly visible within 100 km from the coast. The isolines of nitrate concentration fit well with the isopycnals except within the upper 40 m.

[29] DOM comes mainly from zooplankton excretion and detritus dissolution. Its concentration is high at the surface and decreases with depth and the proximity of the shore. The detritus distribution is similar to that of zooplankton. The ammonium concentration displays a subsurface maximum just below the euphotic depth, between 40 m and 80 m (around  $0.6 \text{ mmolN/m}^3$ ), corresponding to the depth range of high regeneration without any light.

[30] These results also point out the different horizontal extension for the different components: nitrate consumption is maximum within 80 km from the coast, phytoplankton bloom is mainly comprised between the coast and

200 km offshore while the zooplankton peak extends further offshore.

### 3.1.3. Mesoscale Structures

[31] We now examine the mesoscale structures that develop in the 3-D simulation (Figure 4). The energetic mesoscale circulation affects both the physical and biogeochemical fields. The SST field is characterized by a succession of cold filaments spreading offshore from the coast (Figure 4a), associated with negative sea level anomalies (Figure 4c) and intense fronts of surface vorticity (Figure 4f). A succession of positive and negative sea level anomalies and positive and negative vertical velocity occur within a 100 km-wide coastal band (Figures 4c, 4d, and 4e). Such an alternation is caused by the instability of the coastal jet [McCreary *et al.*, 1991; Barth, 1994]. During the simulation, the number of positive and negative anomalies of vertical velocity and sea level varies between 3 and 4. The wave length of the instability is thus in the range 100–150 km, which is consistent with the typical scales of the baroclinic instability of coastal upwelling jets [Barth, 1994]. Figure 4 displays a situation with 4 structures for a 400 km long basin. The magnitude of the negative vertical velocity in the cold filament is 10–20 m/d, in agreement with the estimations from observations of Flament *et al.* [1985] and Kadko *et al.* [1991] for the Californian EBUS. Further offshore, larger structures can be observed from 150 km to 500 km from the coast. The diameter of the largest structure is

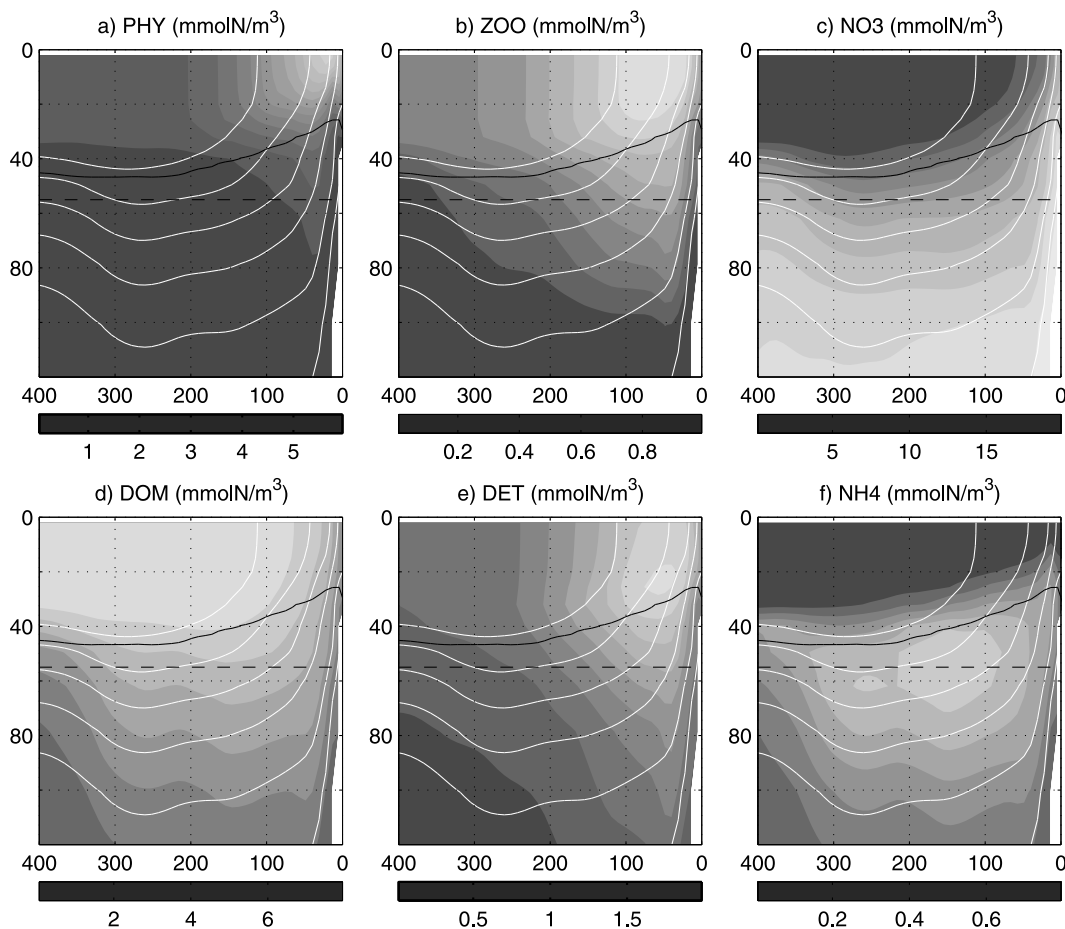


**Figure 3.** Time and alongshore-averaged biogeochemical fields: (a) phytoplankton, (b) zooplankton, (c) nitrate, (d) dissolved organic matter, (e) detritus, and (f) ammonium. The white lines are the isopycnals, the dashed black lines mark the upper 55 m and the solid black lines indicate the  $0.005 \text{ mmolN/m}^3/\text{d}$  isolines of primary production as a proxy of the euphotic depth. The data originate from the fifth year.

approximately 200 km, in agreement with the typical size of eddy diameter observed in altimeter data at this latitude.

[32] All the simulated structures smaller or equal to mesoscale will be referred to as mesoscale structures in the following. This denomination thus includes mesoscale eddies, meanders that emerge from baroclinic instability, filament and near-inertial waves. This mesoscale dynamics has a strong signature on the biogeochemical components of the ecosystem, both in the surface layer (0–55 m, Figures 4g–4l) and below (55–150 m, Figures 4m–4r). Both the mesoscale structures close to the coast and the larger scale eddies display a clear signature on the surface ecosystem fields. The surface nitrate distribution is very well anti-correlated with that of SST. The nitrate concentration is high in the coastal jet and in the filaments (more than  $2 \text{ mmolN/m}^3$ ). In contrast, phytoplankton, zooplankton and detritus concentrations are also high in the filaments (respectively approximately  $3 \text{ mmolN/m}^3$ ,  $1 \text{ mmolN/m}^3$  and  $2 \text{ mmolN/m}^3$ ) but are rather weak within the coastal jet (approximately  $1 \text{ mmolN/m}^3$ ,  $0.4 \text{ mmolN/m}^3$  and  $0.8 \text{ mmolN/m}^3$ , Figures 4h, 4i, and 4k).

[33] In the subsurface layer (55–150 m), the signature of the mesoscale dynamics is also clearly visible in all ecosystem fields (Figures 4m–4r). Patches of high phyto-

plankton concentration are localized below the cold filaments (Figure 4n). Patches of high zooplankton concentration are found not only below the cold filament but also around anticyclonic structures located 100–150 km offshore (Figure 4o). The nitrate concentration is higher along the slope than further offshore in relation with coastal upwelling (Figure 4m). A minimum of nitrate between 200–300 km offshore within an eddy is associated with the deepening of the isopycnals in this anticyclonic eddy. Such a signature of mesoscale eddy is also visible on DOM and ammonium (Figures 4p and 4r).

### 3.2. Differences Between the Two Simulations

[34] In order to examine the role of the mesoscale variations in the structure of the ecosystem, the 3-D simulation is compared with the 2-D simulation, which excludes mesoscale variations (see section 2.3). The main aspects that are examined in the following are the differences in biogeochemical stocks, in nutrient input, in primary production and in export.

[35] Mesoscale dynamics is expected to redistribute the biogeochemical material horizontally between the coast and the open ocean. This effect is investigated by displaying cross-shore-averaged profiles (Figure 5). Moreover, the

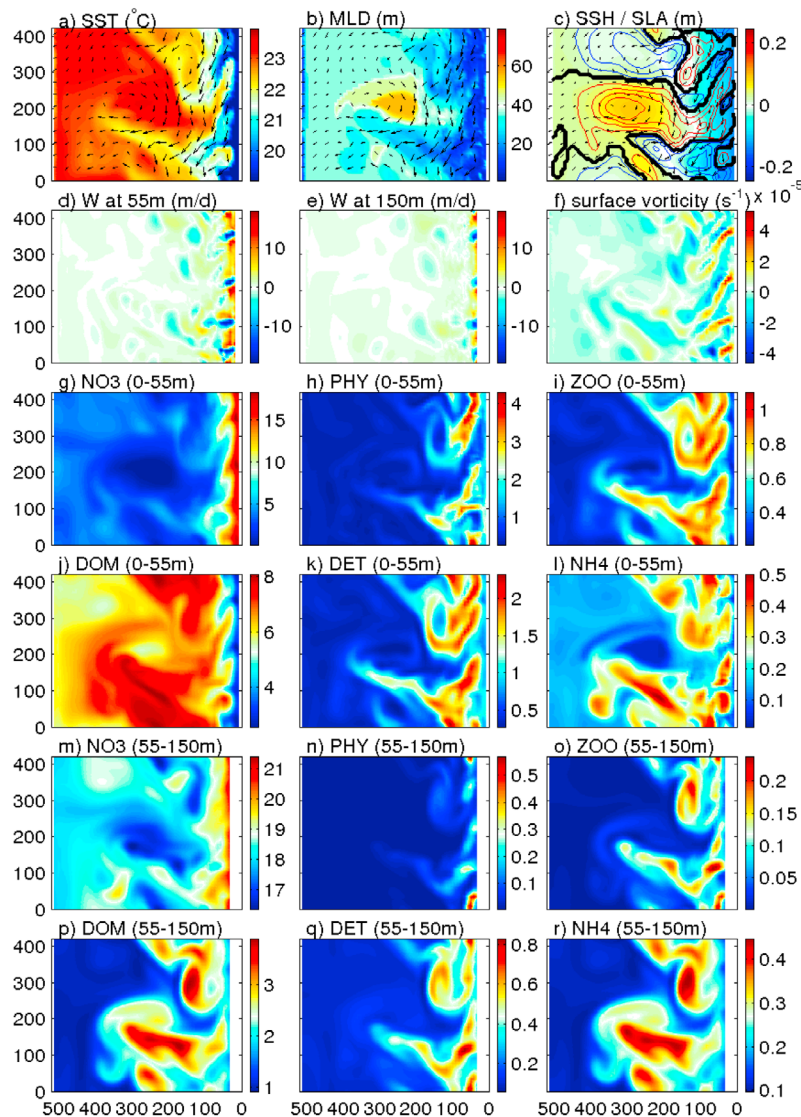


**Figure 4.** Snapshots (3 days average) of (a) SST ( $^{\circ}\text{C}$ ), (b) mixed layer depth (m), and (c) sea surface height (m). Contours of positive (negative) sea level anomaly are indicated in red (blue). (d) Vertical velocity at 55m (m/d), (e) vertical velocity at 150m (m/d), and (f) surface vorticity ( $\text{s}^{-1}$ ). (g–l) Concentrations of biogeochemical components averaged within the upper 55 m, and (m–r) concentrations of biogeochemical component average within the 55–150 m layer. Surface horizontal velocity field is indicated on Figures 4a, 4b, and 4c by arrows.

redistribution by the mesoscale circulation is also expected to impact the integrated stocks and fluxes within the coastal region. To study this aspect, a biogeochemical budget of every component has been performed within the coastal transition zone box (Figure 6). The most fundamental aspects of this budget are detailed in the following.

### 3.2.1. Impact of Mesoscale Circulation on Phytoplankton and Zooplankton

[36] Figure 5a shows the cross-shore profile of surface phytoplankton concentration with and without mesoscale variations. A phytoplankton bloom occurs in both simulations in a coastal band within 200 km from the coast, but the amplitude of the phytoplankton peak differs: In 3-D, the maximum phytoplankton concentration is  $2.2 \text{ mmolN/m}^3$ , whereas it doubles in 2-D ( $4.5 \text{ mmolN/m}^3$ ). The phyto-

plankton concentration is similar near the coast ( $1.8 \text{ mmolN/m}^3$  in 3-D compared with  $1.6 \text{ mmolN/m}^3$  in 2-D), whereas, between 120 km and 230 km offshore, phytoplankton concentration is higher in 3-D than in 2-D. The offshore extension of the phytoplankton bloom, defined by the distance where phytoplankton concentration reaches its offshore value, is approximately 200 km in the 3-D simulation and only 120 km in the 2-D simulation. Moreover, the total stock of phytoplankton in the CTZ box is weaker by 17% in the 3-D simulation ( $19.0 \text{ kmolN/m}$  in 3-D and  $22.8 \text{ kmolN/m}$  in 2-D, Figure 6b).

[37] The zooplankton cross-shore profile is very similar to the phytoplankton's (Figure 5b). As for phytoplankton, the zooplankton stock in the CTZ box is 8% weaker in 3-D ( $9.8 \text{ kmolN/m}$ ) than in 2-D ( $10.7 \text{ kmolN/m}$ , Figure 6c).

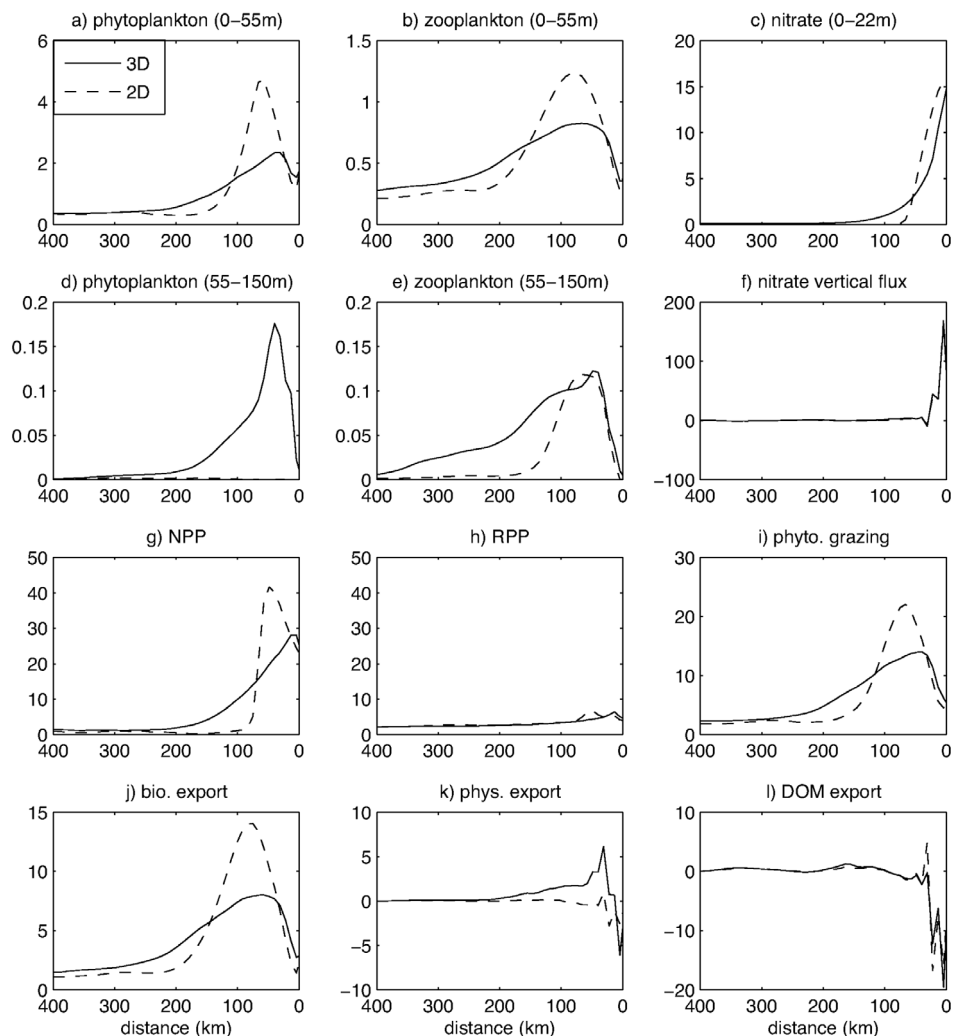


**Figure 5.** (a) Phytoplankton and (b) zooplankton concentration averaged within the upper 55m ( $\text{mmolN/m}^3$ ), and (c) nitrate concentration averaged within the upper 22m ( $\text{mmolN/m}^3$ ). (d) Phytoplankton and (e) zooplankton concentration, averaged between 55m and 150m ( $\text{mmolN/m}^3$ ), (f) nitrate vertical flux at 55m ( $\text{mmolN/m}^2/\text{d}$ ), (g) NPP, (h) RPP, (i) phytoplankton grazing by zooplankton ( $\text{mmolN/m}^2/\text{day}$ ), (j) biological export (fast-sinking particles and detritus sink), (k) physical export (downward flux at 55m of phytoplankton, zooplankton and detritus), and (l) downward flux of dissolved organic matter ( $\text{mmolN/m}^2/\text{s}$ ) for the 3-D (solid line) and 2-D (dashed line) simulations.

[38] Those results raise two questions: first, why is the phytoplankton peak weaker and the offshore extension greater in the 3-D simulation? Second, why is the phytoplankton integrated content reduced in the CTZ box? To investigate this matter, we analyze how the phytoplankton stock is sustained, by examining the nutrient concentration and the primary production.

### 3.2.2. Impact of Mesoscale Circulation on Nutrient Input and Primary Production

[39] Concerning the nitrate budget in the CTZ box, the nitrate input including advection and diffusion is similar in 2-D and 3-D, as expected by construction (Figure 6a). But we have found that the horizontal cross-shore distribution of nitrate concentration is different, with a wider nutrient-rich coastal band in 3-D: in 2-D, the upper 22 m are nitrate-depleted 70 km offshore. In 3-D, the nitrate concentration

within the upper 22 m decreases more rapidly than in 2-D within 50 km from the coast, but more slowly further offshore. As a consequence, the upper 22 m are nitrate-depleted only 150 km offshore.

[40] Primary production is dominated by new primary production (NP, Figures 5g and 5h). The total NPP in the CTZ box is very similar in both runs, with  $2749 \text{ molN/m}^2/\text{d}$  in 3-D and  $2690 \text{ molN/m}^2/\text{d}$  in 2-D (Figure 6b). However the localization of the NPP is different in both runs. In 3-D, NPP is maximal at the coast ( $28 \text{ mmolN/m}^2/\text{d}$ ), then decreases to reach an offshore value below  $2 \text{ mmolN/m}^2/\text{d}$  200 km offshore (Figure 5g). In contrast, the NPP in 2-D increases from  $25 \text{ mmolN/m}^2/\text{d}$  at the coast to  $40 \text{ mmolN/m}^2/\text{d}$  50 km offshore and decreases very sharply to reach its offshore minimum value 80 km offshore. Note that in 2-D, the sharp decrease in NPP (Figure 5g), the depletion in nitrate

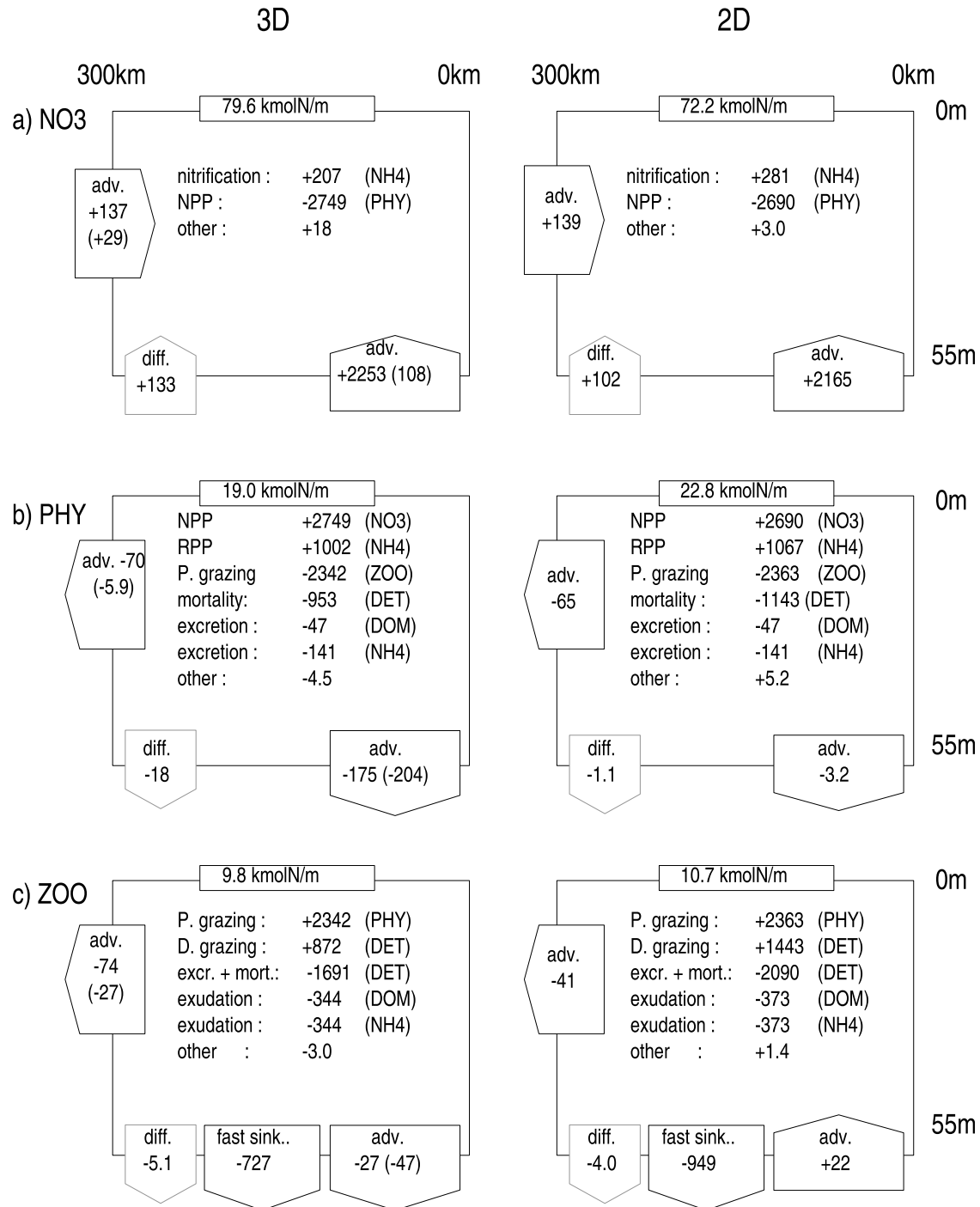


**Figure 6.** Budget in the CTZ box (see section 2.3) for (a) nitrate, (b) phytoplankton, (c) zooplankton, (d) detritus, (e) dissolved organic matter, and (f) ammonium in the (left) 3-D and (right) 2-D runs (mmolN/m<sup>3</sup>). The source terms are positive and the origin component is indicated in parentheses. The sink terms are negative and the destination component is indicated in parentheses. The term called “other” is the sum of the other terms (numerical correction, trend due to the assimilation filter of the temporal scheme, internal damping, dilution effects and so on). The two vertical arrows are diffusion (left) and advection (right). The horizontal arrow is horizontal advection across the western boundary of the CTZ box. The contribution of the Reynolds averaged fluxes to the total advective fluxes are indicated in parentheses for the 3-D run.

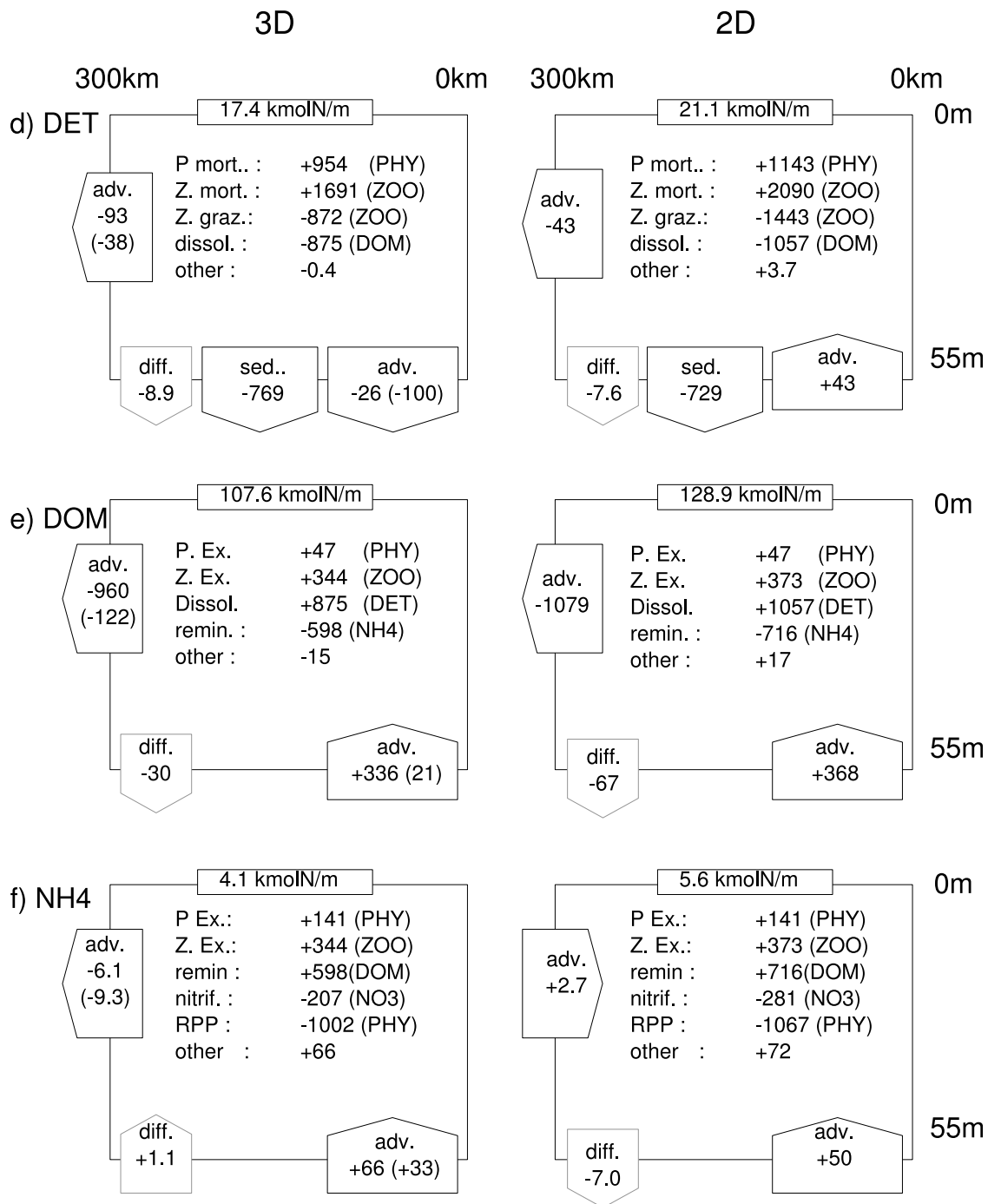


Figure 6. (continued)

(Figure 5c) and the phytoplankton maximum (Figure 5a) are collocated. NPP is thus more intense within 80 km from the coast in 2-D, which explains the stronger phytoplankton peak.

[41] In brief, the differences in phytoplankton cross-shore distribution are well elucidated by the cross-shore profiles of NPP and nitrate. Conversely, as the total nutrient input and NPP are very similar in both runs, the strong difference in

phytoplankton stock cannot be explained by a difference in the nutrient input. Others processes need to be investigated.

### 3.2.3. Differences in Pathways for Export

[42] We now investigate how the nitrogen brought into the surface layer by upwelling is exported offshore and downward. Since the system is stationary, the nitrate input into the CTZ box is compensated by the offshore export of organic matter at its offshore boundary and by the downward export at 55 m. Also, since nitrate input is similar in

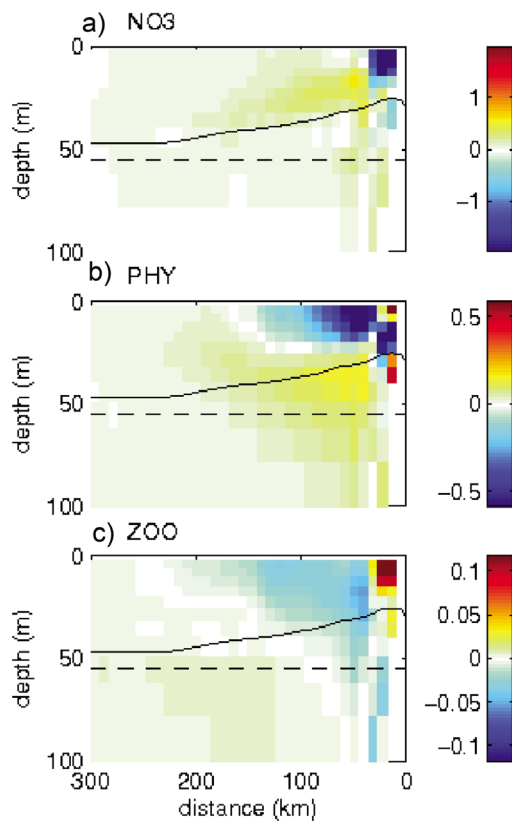


**Figure 7.** Opposite of the divergence of the Reynolds-averaged fluxes for (a) nitrate, (b) phytoplankton, and (c) zooplankton concentration, in the 3-D simulation ( $\text{mmolN/m}^3$ ). The solid black line is the euphotic depth. The dashed line indicates the vertical boundary of the CTZ box (55 m).

the two runs, so is the total export. However, the main pathways for export are different.

[43] The most striking difference between the two simulations is the contribution to total export of the transport of phytoplankton and more generally of particulate organic matter (phytoplankton, zooplankton and detritus) out of the CTZ box. The sum of these contributions is  $497 \text{ molN/m}^3/\text{d}$  in 3-D (19% of total export) and only  $100 \text{ molN/m}^3/\text{d}$  in 2-D (4% of total export). The largest contribution to the difference of export is actually the difference in phytoplankton vertical advection ( $-175 \text{ molN/m}^3/\text{d}$  in 3-D, but only  $-3.2 \text{ molN/m}^3/\text{d}$  in 2-D). This strongly affects the subsurface phytoplankton concentration, which peaks up to  $0.18 \text{ mmolN/m}^3$  in 3-D at 50 km from the coast within the 55–150 m layer, in contrast with the concentration in 2-D not exceeding  $0.01 \text{ mmolN/m}^3$  (Figure 5d). In this layer, phytoplankton comes from the upper layer since there is no primary production below the euphotic layer (Figure 3). The vertical export of phytoplankton is a fundamental difference between the two runs. The eddy contributions to the advective fluxes (indicated into parentheses on the biogeochemical budget (Figure 6)), clearly indicate that the phytoplankton vertical flux of the 3-D simulation is driven by the phytoplankton vertical Reynolds-averaged flux ( $-204 \text{ molN/m}^3/\text{d}$ ). Similarly, the zooplankton vertical flux is predominately driven by the eddy flux ( $-47 \text{ molN/m}^3/\text{d}$ ). Note that the contributions of the mean

flow to vertical advective fluxes are different in the two simulations (for phytoplankton  $-3.2 \text{ molN/m}^3/\text{d}$  in 2-D and  $+29 \text{ molN/m}^3/\text{d}$  in 3-D). The main reason is that the distribution of tracers are different, with, for instance, more phytoplankton in subsurface. Another reason is the variation of the vertical velocity sign along the bottom boundary of the CTZ box. An approach based on an isopycnal bottom boundary and a mean flow defined along isopycnal surfaces would improve the comparison on this point.

[44] The organic matter content is weaker in 3-D. This results in a weaker export by fast-sinking particles and by the transport of DOM out of the CTZ box. The fast-sinking flux mediated by zooplankton (see Appendix A) is indeed weaker in 3-D ( $-727 \text{ molN/m}^3/\text{d}$ ) than in 2-D ( $-949 \text{ molN/m}^3/\text{d}$ , Figure 6c). The net flux of DOM across the boundary of the CTZ box is weaker in 3-D ( $-654 \text{ molN/m}^3/\text{d}$ ) than in 2-D ( $-778 \text{ molN/m}^3/\text{d}$ ). These reduced export terms in 3-D compensate the differences of particulate organic matter export. The total export is fairly constant but the nature of export differs.

### 3.2.4. Analysis of the Reynolds-Averaged Fluxes in 3-D

[45] The cross-shore and vertical structure of the redistribution of biogeochemical materials is now examined in more details. For that purpose, the convergence of the Reynolds-averaged fluxes has been computed for the phytoplankton, zooplankton and nitrate fields and is shown on Figure 7.

[46] Nitrate Reynolds fluxes tend to decrease nitrate at the surface near the shore (Figures 7b and 7c). The negative nitrate trend is more than  $2 \text{ mmolN/m}^3/\text{d}$  (Figure 7a), the same magnitude as NPP within the upper 10 m.

[47] The phytoplankton Reynolds fluxes show a downward export. Phytoplankton is removed from the upper 20 m and redistributed in a subsurface layer between 30 m and 100 m. This occurs between 30 km and 150 km from the coast and is mainly driven by the vertical deposit. The vertical velocities are particularly efficient for downward export since exported phytoplankton cannot survive without light. Thus, an upward flux cannot import a large phytoplankton biomass into the mixed layer. Near the coast, phytoplankton eddy fluxes tend to enrich the coastal zone at the surface but also to remove phytoplankton in subsurface along the continental slope. The phytoplankton trend associated with the Reynolds fluxes varies between  $-0.5 \text{ mmolN/m}^3/\text{d}$  in the mixed layer and  $0.2 \text{ mmolN/m}^3/\text{d}$ . This is less than the nitrate trend due to eddies. The phytoplankton contribution to nitrogen redistribution by eddies is thus less important than the nitrate one.

[48] The Reynolds-averaged fluxes of zooplankton tend to increase the zooplankton concentration within the upper 30 m between the coast and 30 km from the coast (Figure 7g). Zooplankton is taken away from almost everywhere to enrich the coastal zone. The Reynolds-averaged fluxes are weaker for zooplankton than for phytoplankton. The maximum zooplankton deposit is  $0.05 \text{ mmolN/m}^3/\text{d}$ . The zooplankton contribution to nitrogen redistribution is very low compared to the nitrate and phytoplankton's ones.

## 4. Discussion

[49] A classical way to investigate the role of mesoscale circulation consists in comparing eddying simulations and

**Table A1a.** Parametrization of the Biological Fluxes

Name	Parametrization
Light limitation	$L_I = 1 - e^{-\frac{PAR}{K_{PAR}}}$
Nitrate limitation	$L_{NO_3} = \frac{NO_3}{NO_3 + K_{NO_3}} e^{-\psi/NH_4}$
Ammonium limitation	$L_{NH_4} = \frac{NH_4}{NH_4 + K_{NH_4}}$
New primary production	$NP = \mu_p L_I L_{NO_3} P$
Regenerated primary production	$RP = \mu_p L_I L_{NH_4} P$
Phytoplankton grazing	$G_p = g_{z_{K_i+pP+(1-p)D}} \frac{pP}{(1-p)D} Z$
Detritus grazing	$G_d = g_{z_{K_i+pP+(1-p)D}} \frac{(1-p)D}{(1-p)D} Z$
Preference for phytoplankton	$p = \frac{pP}{pP+(1-p)D}$
Phytoplankton mortality	$M_p = m_p P$
Zooplankton mortality	$M_z = m_z Z^2$
Zooplankton exudation	$E_z = \mu_z Z$
Remineralization of DOM	$M_{dom} = \mu_{dom} DOM$
Nitrification	$M_n = \mu_n NH_4$

simulations with a low horizontal resolution or with a high viscosity. This method was intensively used to examine the role of mesoscale activity on primary production in the open ocean, where it is now well established that marine ecosystems are sensitive to the mesoscale dynamics (see Lévy [2008] for a review). In most cases in the open ocean, the intensification of turbulence was found to enhance primary production and increase the phytoplankton content. The leading process for this enhancement is the upwelling of nutrients associated with the mesoscale and submesoscale activity [McGillicuddy *et al.*, 1998; Lévy *et al.*, 2001b]. EBUSs differ from open ocean by the higher richness in nutrient driven by coastal upwelling. In this context, eddy activity tends to flatten the nutricline. A study based on observations or on simulations with different horizontal resolutions [Lachkar *et al.*, 2009] would not allow to separate the effect we investigated from the change in nutrient input associated with the change in mean circulation. Thus the classical approach in the open ocean does not allow to fully address the role of mesoscale dynamics, since it does not hold constant the environmental conditions, that are crucial in the context of EBUSs. In this paper, the rectification of the mean flow and its impact on nutrient input by the mesoscale dynamics is not addressed and the method is devoted to examine the differences that emerge under constant mean flow and nutrient input.

## 5. Summary

[50] An idealized model of coastal upwelling has been built to address the impact of mesoscale variations on coastal upwelling ecosystems. It mimics an infinite straight meridionally-oriented coast using cyclic north–south boundary conditions. A parametrization of the onshore flow in the thermocline has been used to realistically reproduce the upwelling circulation. It consists in the introduction of an additional alongshore pressure gradient representing the meridional slope of the thermocline. The associated geostrophic flow balances the offshore surface Ekman flow. 5-year simulations have been carried out and provide a mean circulation in a quasi-equilibrated state. On the basis of observations in EBUS, the circulation is typical of coastal

upwelling with an equatorward coastal jet, a poleward undercurrent, a suitable mesoscale circulation, and upwelling source waters having realistic temperature and salinity characteristics.

[51] An originality of the study is to compare simulations including and excluding the presence of features emerging from mesoscale dynamics with fairly constant nutrient input by coastal upwelling. Practically, an eddy simulation (3-D) is contrasted to a non-eddy simulation (2-D) having exactly the same Eulerian meridional and temporal mean circulation. This results in the two simulations having the same upwelling mass flux and upwelled waters having similar properties. Strong differences have been found between the two simulations. The offshore extension of the phytoplankton bloom is increased from 120 km to 200 km by the presence of mesoscale structures. The localization of NPP is highly contrasted. In 2-D, NPP is confined to a 80 km wide coastal band whereas NPP is distributed over a 200 km-wide coastal band in 3-D. Mesoscale circulation and in particular filaments export offshore nitrate and phytoplankton and result in the spreading of NPP and thus of other biogeochemical properties.

[52] A biogeochemical budget has been carried out between 0 and 55 m in a 300 km-wide coastal box (CTZ box) and provides evidence of a reduced total phytoplankton stock in the 3-D simulation compared to the 2-D simulation (−17%). The nutrient input and the total primary production are very close in both runs and cannot explain the difference in phytoplankton content in the CTZ box. Conversely, a strong downward export of phytoplankton driven by eddies and filaments contributes to reduce the phytoplankton content. The analysis of the different terms contributing to export shows the major role of vertical transport of phytoplankton, zooplankton and detritus in 3-D. In this simulation, 19% of organic matter is exported out of the CTZ box by this term, whereas only 4% of organic matter is exported by transport of phytoplankton, zooplankton and detritus in the non-eddy simulation. Our results emphasize the impact of the subduction of phytoplankton-rich waters on biogeochemical budget.

[53] The analysis of the eddy fluxes shows the deposit of biogeochemical materials by the eddies. Eddies redistribute nitrate from the top 20 m in the coastal region to the subsurface (10–50 m) further offshore. Phytoplankton tends to be exported from the upper 20 m to the 30–80 m deep layer. Eddies tend to enrich the coastal region in zooplankton, while upwelling flow advects zooplankton-poor waters in this region.

[54] A limitation is to neglect the meridional variation of the Coriolis factor, due to the north–south cyclic boundary conditions imposed by our model configuration. This meridional variation is responsible for the westward propagation of eddies and Rossby waves and may affect the stability of coastal currents [Hristova *et al.*, 2008]. Those processes may enhance the offshore export of biogeochemical materials in EBUS. The study of such a process is beyond the scope of this study. Future work aimed at investigating this process requires the development of a different model configuration with western, northern and southern open boundaries, which implies alongshore varia-

**Table A1b.** Parameters of the Biological Model

Name	Value
Nutrient limitation half saturation	$K_{NO_3} = 0.7 \text{ mmolN/m}^3$
Ammonium limitation half saturation	$K_{NH_4} = 0.1 \text{ mmolN/m}^3$
Inhibition of nitrate uptake by Ammonium	$\psi = 3$
Light limitation half-saturation	$K_{PAR} = 33 \text{ W.m}^{-2}$
Phytoplankton maximal growth rate	$\mu_p = 1.5 \text{ d}^{-1}$
Phytoplankton exudation rate	$\gamma = 0.05$
Phytoplankton mortality rate	$m_p = 0.05 \text{ d}^{-1}$
Grazing half-saturation	$K_z = 1 \text{ mmolN/m}^3$
Zooplankton maximal growth rate	$g_z = 0.6 \text{ d}^{-1}$
Assimilated food fraction by zooplankton	$a_z = 0.7$
Preference for phytoplankton	$\tilde{p} = 0.8$
Zooplankton excretion rate	$\mu_z = 0.07 \text{ d}^{-1}$
NH4 fraction of zooplankton excretion	$\alpha_z = 0.5$
Zooplankton mortality rate	$m_z = 0.2 \text{ d}^{-1} \cdot \text{mmolN}^{-1} \cdot \text{m}^3$
Fraction of slow sinking mortality	$f_z = 0.5$
Nitrification rate	$\mu_n = 0.05 \text{ d}^{-1}$
DOM breakdown rate	$\mu_{dom} = 0.0056 \text{ d}^{-1}$
NH4 fraction of detritus dissolution	$\alpha_d = 0$
Detritus sedimentation speed	$V_d = 3 \text{ m.d}^{-1}$
Detritus remineralization rate	$\mu_d = 0.05 \text{ d}^{-1}$
C/N Redfield ratio for phytoplankton	$Rd_{phy} = 6.56 \text{ molC.molN}^{-1}$
C:Chl ratio	$R_{C:Chl} = 60 \text{ mgC.mgChl}^{-1}$

tions of the model variables and increases the complexity of the analysis.

## Appendix A: LOBSTER Ecosystem Model

[55] In this section, details about the ecosystem model are given. The model contains 6 prognostic variables expressed in terms of their nitrogen content: nitrate ( $NO_3$ ), ammonium ( $NH_4$ ), phytoplankton (P), zooplankton (Z), detritus (D) and dissolved organic matter (DOM). The tracers are advected and diffused to mimic the transport by the flow. The biogeochemical interaction are represented by sources and sinks S. The general equation resolved by the numerical ecosystem model for every tracer C is thus

$$\frac{\partial C}{\partial t} = -\nabla(uC) + \text{diff}(C) + S(C).$$

[56] In this equation,  $u$  is the three-dimensional velocity field and  $\text{diff}$  is the diffusion operator. The domain is decomposed into a surface biological layer (0–120 m) and a deep layer (below 120 m). In the deep layer, the biogeochemical interactions are simplified and only a remineralization of all variables in nitrate occurs. In the biological layer, the source and sink (S) term are the following:

$$S(NO_3) = -NP + M_n$$

$$S(P) = (1 - \gamma)(NP + RP) - M_p - G_p$$

$$S(Z) = a_z(G_p + G_d) - M_z - E_z$$

$$S(D) = (1 - a_z)(G_p + G_d) + M_p + f_z M_z - G_d - M_d - V_d \partial_z D$$

$$S(DOM) = \gamma(1 - a_p)(NP + RP) + (1 - \alpha_z)E_z + (1 - \alpha_d)M_d - M_{dom}$$

$$S(NH_4) = -RP - M_n + \gamma\alpha_p(NP + RP) + \alpha_z E_z + \alpha_d M_d + M_{dom}.$$

[57] The different terms are detailed in Tables A1a and A1b. Part of the nitrogen ( $(1 - f_z)m_z Z^2$ ) is instantaneously exported downward and remineralized in nitrate in the

interior of the ocean. This export is called fast-sinking particles. The second way to export down nitrogen in the source and sink terms is the slow sink of detritus represented by the term  $-V_d \partial_z D$ .

[58] **Acknowledgments.** The work of Cyril Lathuilière is supported by DGA. The authors gratefully acknowledge INSU, LEFE-CYBER, MERCATOR and CNES for the additional financial support. This is a contribution to the TWISTED and INTERUP projects.

## References

- Allen, J. S., P. A. Newberger, and J. Federiuk (1995), Upwelling circulation on the Oregon continental shelf. Part I: Response to idealized forcing, *J. Phys. Oceanogr.*, *25*, 1843–1866.
- Barth, J. A. (1994), Short-wavelength instabilities on coastal jets and fronts, *J. Geophys. Res.*, *99*(C8), 16,095–16,115.
- Barton, E. D. (1998), Eastern boundary of the North Atlantic: Northwest Africa and Iberia, in *The Sea*, vol. 11, edited by A. R. Robinson and K. H. Brink, pp. 633–657, John Wiley, New York.
- Blanke, B., and P. Delecluse (1993), Variability of the tropical Atlantic Ocean simulated by a general circulation model with two different mixed-layer physics, *J. Phys. Oceanogr.*, *23*, 1363–1388, doi:10.1175/1520-0485.
- Bricaud, A., A. Morel, and J.-M. André (1987), Spatial/temporal variability of algal biomass and potential productivity in the Mauritanian upwelling zone, as estimated from CZCS data, *Adv. Space Res.*, *7*(2), 53–62.
- Capet, X., J. C. McWilliams, M. J. Molemaker, and A. Shchepetkin (2008), The transition from mesoscale to submesoscale in the California Current System: Flow structure, eddy flux and observational test, *J. Phys. Oceanogr.*, *38*, 29–43, doi:10.1175/2007JPO3671.1.
- Carr, M.-E., and E. Kearns (2003), Production regimes in four Eastern Boundary Current systems, *Deep Sea Res. Part II*, *50*(22–26), 3199–3221.
- Chavez, F. P., R. T. Barber, P. M. Kosro, A. Huyer, S. R. Ramp, T. P. Stanton, and B. Rojas de Mendiola (1991), Horizontal transport and the distribution of nutrients in the coastal transition zone off northern California: Effects on primary production, phytoplankton biomass and species composition, *J. Geophys. Res.*, *96*(C8), 14,833–14,848.
- de Boyer Montégut, C., A. S. Fischer, G. Madec, A. Lazar, and D. Iudicone (2004), Mixed layer depth over the global ocean: An examination of profile data and a profile-based climatology, *J. Geophys. Res.*, *109*, C12003, doi:10.1029/2004JC002378.
- Durski, S. M., and J. S. Allen (2005), Finite-amplitude evolution of instabilities associated with the coastal upwelling front, *J. Phys. Oceanogr.*, *35*, 1606–1628.
- Edwards, C. A., H. P. Batchelder, and T. M. Powell (2000), Modeling microzooplankton and macrozooplankton dynamics within a coastal upwelling system, *J. Plankton Res.*, *22*(9), 1619–1648.
- Flament, P., L. Armi, and L. Washburn (1985), The evolving structure of an upwelling filament, *J. Geophys. Res.*, *90*(C6), 11,765–11,778.
- Gruber, N., H. Frenzel, S. C. Doney, P. Marchesiello, J. C. McWilliams, J. R. Moisan, J. J. Oram, G.-K. Plattner, and K. D. Stolzenbach (2006), Eddy-resolving simulation of plankton ecosystem dynamics in the California Current System, *Deep Sea Res. Part I*, *53*(9), 1483–1516, doi:10.1016/j.dsr.2006.06.005.
- Hristova, H. G., J. Pedlosky, and M. A. Spall (2008), Radiating instability of a meridional boundary current, *J. Phys. Oceanogr.*, *38*, 2294–2307, doi:10.1175/2008JPO3853.1.
- Hurlburt, H. E., and J. D. Thompson (1973), Coastal upwelling on a beta-plane, *J. Phys. Oceanogr.*, *3*, 16–32.
- Kadko, D. C., L. Washburn, and B. Jones (1991), Evidence of subduction within cold filaments of the northern California coastal transition zone, *J. Geophys. Res.*, *96*(C8), 14,909–14,926.
- Krémeur, A.-S., M. Lévy, O. Aumont, and G. Reverdin (2009), Impact of the subtropical mode water biogeochemical properties on primary production in the North Atlantic: New insights from an idealized model study, *J. Geophys. Res.*, *114*, C07019, doi:10.1029/2008JC005161.
- Lachkar, Z., N. Gruber, G. K. Plattner, and C. Hauri (2009), The future coastal ocean: The impact of ocean acidification and wind changes on coastal productivity and carbon cycling, paper presented at Aquatic Sciences Meeting 2009, Adv. the Sci. of Limnol. and Oceanogr., Nice, France, 25–30 Jan.
- Lathuilière, C., V. Echevin, and M. Lévy (2008), Seasonal and intraseasonal surface chlorophyll-a variability along the northwest African coast, *J. Geophys. Res.*, *113*, C05007, doi:10.1029/2007JC004433.
- Lentz, S. J., and D. C. Chapman (2004), The importance of nonlinear cross-shelf momentum flux during wind-driven coastal upwelling, *J. Phys. Oceanogr.*, *34*, 2444–2457.

- Lévy, M. (2008), The modulation of biological production by oceanic mesoscale turbulence, *Lect. Notes Phys.*, 744, 219–261, doi:10.1007/978-3-540-75215-89.
- Lévy, M., A. Estubier, and G. Madec (2001a), Choice of an advection scheme for biogeochemical models, *Geophys. Res. Lett.*, 28, 3725–3728.
- Lévy, M., P. Klein, and A.-M. Treguier (2001b), Impacts of sub-mesoscale physics on phytoplankton production and subduction, *J. Mar. Res.*, 59, 535–565, doi:10.1357/002224001762842181.
- Lévy, M., Y. Lehahn, J.-M. André, L. Mémerly, H. Loisel, and E. Heifetz (2005), Production regimes in the Northeast Atlantic: A study based on SeaWiFS chlorophyll and OGCM mixed-layer depth, *J. Geophys. Res.*, 110, C07S10, doi:10.1029/2004JC002771.
- Madec, G. (2008), NEMO ocean engine, *Note Pole Model*, 27, Inst. Pierre-Simon Laplace, Paris.
- Madec, G., P. Delecluse, M. Imbard, and C. Lévy (1998), OPA 8.1 ocean general circulation model reference manual, *Note Pole Model*, 11, 91 pp., Inst. Pierre-Simon Laplace, Paris.
- Marchesiello, P., J. C. McWilliams, and A. Shchepetkin (2003), Equilibrium structure and dynamics of the California Current System, *J. Phys. Oceanogr.*, 33, 753–783.
- McCreary, J. P., Y. Fukumachi, and P. Kundu (1991), A numerical investigation of jets and eddies near an eastern ocean boundary, *J. Geophys. Res.*, 96(C2), 2515–2534.
- McGillicuddy, D. J., Jr., A. R. Robinson, D. A. Siegel, H. W. Jannasch, R. Johnson, T. D. Dickey, J. McNeil, A. F. Michaels, and A. H. Knap (1998), Influence of mesoscale eddies on new production in the Sargasso Sea, *Nature*, 394, 263–266.
- Nykjaer, L., and L. Van Camp (1994), Seasonal and interannual variability of coastal upwelling along northwest Africa and Portugal from 1981 to 1991, *J. Geophys. Res.*, 99(C7), 14,197–14,207.
- Pacanowski, R. C., and A. Gnanadesikan (1998), Transient response in a Z-level ocean model that resolves topography with partial cells, *Mon. Weather Rev.*, 126(12), 3248–3270.
- Penven, P., V. Echevin, J. Pasapera, F. Colas, and J. Tam (2005), Average circulation, seasonal cycle, and mesoscale dynamics of the Peru Current System: A modeling approach, *J. Geophys. Res.*, 110, C10021, doi:10.1029/2005JC002945.
- Philander, S. G. H., and J.-H. Yoon (1982), Eastern boundary currents and coastal upwelling, *J. Phys. Oceanogr.*, 12, 862–879.
- Rossi, V., C. López, J. Sudre, E. Hernández-García, and V. Garçon (2008), Comparative study of mixing and biological activity of the Benguela and Canary upwelling systems, *Geophys. Res. Lett.*, 35, L11602, doi:10.1029/2008GL033610.
- Spitz, Y. H., P. A. Newberger, and J. S. Allen (2003), Ecosystem response to upwelling off Oregon coast: Behavior of three nitrogen-based models, *J. Geophys. Res.*, 108(C3), 3062, doi:10.1029/2001JC001181.
- Spitz, Y. H., J. S. Allen, and J. Gan (2005), Modeling of ecosystem processes on the Oregon shelf during the 2001 summer upwelling, *J. Geophys. Res.*, 110, C10S17, doi:10.1029/2005JC002870.
- Treguier, A. M., B. Barnier, A. P. de Miranda, J. M. Molines, N. Grima, M. Imbard, G. Madec, C. Messenger, T. Reynaud, and S. Michel (2001), An eddy-permitting model of the Atlantic circulation: Evaluating open boundary conditions, *J. Geophys. Res.*, 106(C10), 22,115–22,129.
- Van Camp, L., L. Nykjaer, E. Mittelstaedt, and P. Schlittenhardt (1991), Upwelling and boundary circulation off northwest Africa as depicted by infrared and visible satellite observations, *Prog. Oceanogr.*, 26, 357–402.
- Zalesak, S. T. (1979), Fully multidimensional flux corrected transport algorithms for fluid, *J. Comput. Phys.*, 31, 335–362.

V. Echevin, M. Lévy, and G. Madec, LOCEAN, Institut Pierre-Simon Laplace, Université Pierre et Marie Curie, CNRS, IRD, MNHN, 4 pl. Jussieu, F-75252 Paris CEDEX 5, France. (vincent.echevin@locean-ipsl.upmc.fr; marina.levy@locean-ipsl.upmc.fr; gurkan.madec@locean-ipsl.upmc.fr)

C. Lathuilière, REC, HOM, SHOM, B.P. 30316, F-29603 Brest, France. (cyril.lathuiliere@shom.fr)